

Research and application of stochastic resonance in quad-stable potential system

Li-Fang He(贺利芳), Qiu-Ling Liu(刘秋玲)†, and Tian-Qi Zhang(张天骐)

Citation: Chin. Phys. B, 2022, 31 (**7**): 070503. DOI: 10.1088/1674-1056/ac4228
Journal homepage: http://cpb.iphy.ac.cn; http://iopscience.iop.org/cpb

What follows is a list of articles you may be interested in

Asymmetric stochastic resonance under non-Gaussian colored noise and time-delayed feedback

Ting-Ting Shi(石婷婷), Xue-Mei Xu(许雪梅), Ke-Hui Sun(孙克辉), Yi-Peng Ding(丁一鹏), Guo-Wei Huang(黄国伟)
Chin. Phys. B, 2020, 29 (**5**): 050501. DOI: 10.1088/1674-1056/ab7e9f

Novel Woods-Saxon stochastic resonance system for weak signal detection

Yong-Hui Zhou(周永辉), Xue-Mei Xu(许雪梅), Lin-Zi Yin(尹林子), Yi-Peng Ding(丁一鹏), Jia-Feng Ding(丁家峰), Ke-Hui Sun(孙克辉)
Chin. Phys. B, 2020, 29 (**4**): 040503. DOI: 10.1088/1674-1056/ab75ca

Stochastic resonance and synchronization behaviors of excitatory-inhibitory small-world network subjected to electromagnetic induction

Xiao-Han Zhang(张晓函), Shen-Quan Liu(刘深泉)
Chin. Phys. B, 2018, 27 (**4**): 040501. DOI: 10.1088/1674-1056/27/4/040501

Analysis of weak signal detection based on tri-stable system under Levy noise

Li-Fang He(贺利芳), Ying-Ying Cui(崔莹莹), Tian-Qi Zhang(张天骐), Gang Zhang(张刚), Ying Song(宋莹)
Chin. Phys. B, 2016, 25 (**6**): 060501. DOI: 10.1088/1674-1056/25/6/060501

A circular zone counting method of identifying a Duffing oscillator state transition and determining the critical value in weak signal detection

Li Meng-Ping, Xu Xue-Mei, Yang Bing-Chu, Ding Jia-Feng
Chin. Phys. B, 2015, 24 (**6**): 060504. DOI: 10.1088/1674-1056/24/6/060504

Research and application of stochastic resonance in quad-stable potential system

Li-Fang He(贺利芳), Qiu-Ling Liu(刘秋玲)†, and Tian-Qi Zhang(张天骐)

School of Communication and Information Engineering, Chongqing University of Posts and Telecommunications (CQUPT), Chongqing 400065, *China*

(Received 19 October 2021; revised manuscript received 16 November 2021; accepted manuscript online 11 December 2021)

To solve the problem of low weak signal enhancement performance in the quad-stable system, a new quad-stable potential stochastic resonance (QSR) is proposed. Firstly, under the condition of adiabatic approximation theory, the stationary probability distribution (SPD), the mean first passage time (MFPT), the work (W), and the power spectrum amplification factor (SAF) are derived, and the impacts of system parameters on them are also extensively analyzed. Secondly, numerical simulations are performed to compare QSR with the classical Tri-stable stochastic resonance (CTSR) by using the genetic algorithm (GA) and the fourth-order Runge–Kutta algorithm. It shows that the signal-to-noise ratio (SNR) and mean signal-to-noise increase (MSNRI) of QSR are higher than CTSR, which indicates that QSR has superior noise immunity than CTSR. Finally, the two systems are applied in the detection of real bearing faults. The experimental results show that QSR is superior to CTSR, which provides a better theoretical significance and reference value for practical engineering application.

Keywords: bearing fault detection, QSR, weak signal detection, SAF, W

PACS: 05.40.–a, 05.45.–a, 05.40.Fb, 02.60.Cb **DOI:** 10.1088/1674-1056/ac4228

1. Introduction

In recent decades, Stochastic Resonance (SR)[1] has been widely studied in physics,[2–4] biology,[5–7] and many other scientific fields.[8–12] SR is a phenomenon showing the fluctuation force acts on the system non-linearly.[13–15] The SR theory was first introduced by Benzi *et al.*[13] in the 1990s while exploring the glacial period. Subsequently, more novel SR theories have emerged. McNamara *et al.*[16,17] proposed adiabatic approximation theory based on transition probability. Due to the limitations of small parameters in the adiabatic approximation theory, Dykman *et al.*[18] proposed the linear response theory to characterize SR more comprehensively. Then, Jung *et al.*[19–21] analyzed the SNR through the Fokker–Planck equation (FPE).

Currently, some of the famous potential function models have emerged from researchers worldwide, including: classical bistable SR,[22–25] exponential bistable SR,[26] coupled bistable SR,[27–29] and other tri-stable and multi-stable potential function models. Tan Chunlin *et al.*[30] presented the application of standard tri-stable SR system in early bearing fault diagnosis. Yang Yulei *et al.*[31] proposed the research on a self-adaptive, cascaded tri-stable SR system under Levy noise. Zhang Bu *et al.*[32] proposed the tri-stable state system powered by additive and multiplicative noise, and studied its mean first passage time (MFPT) and steady-state probability density (SPD). Li *et al.*[33] proposed an adjustable steady-state system and concluded that there were various nonlinear potential functions in the tri-stable system. Subsequently, researchers have successively studied the compound tri-stable potential function,[34] *etc*. In addition, there are also lots of novel SR, such as fractional SR,[35,36] stable-matching SR[37] and even SR-based signal decomposition.[38] There have been extensive researchers performed on the application of SR in bearing fault diagnosis. For example, Liu *et al.*[39] converted large frequency signals into small frequency signals through the frequency domain information exchange method.

Although researchers have studied the bistable and tri-stable systems from various aspects, there are still few studies on quad-stable or even multi-stable systems, which need further research. In this paper, a new Quad-stable potential stochastic resonance (QSR) is submitted. The structure in this paper is as follows: In Section 2, a system model is proposed and compared with CTSR. Additionally, the expressions of SPD, MFPT, W, and SAF are derived. In Section 3, QSR is compared with CTSR through numerical simulation under low-frequency, high-frequency, and multi-frequency signal conditions. And the variation of SNR and MSNRI is investigated with noise intensity D for two systems. In Section 4, 6205-2RS JEM SKF and HRB 6205-2Z models are chosen for bearing fault detection. Finally, the conclusions of this paper are presented in Section 5.

2. QSR analysis

2.1. Introductions on QSR

Under the over-damping condition, the dynamic Langevin equation of SR can be obtained:

$$\frac{\mathrm{d}x}{\mathrm{d}t} = -\frac{\partial U(x,t)}{\partial x} + \zeta(t), \tag{1}$$

†Corresponding author. E-mail: 1216881140@qq.com

© 2022 Chinese Physical Society and IOP Publishing Ltd

where, $\zeta(t)$ is the Gaussian white noise with $\langle\zeta(t)\rangle = 0$, $\langle\zeta(t)\zeta(t-t')\rangle = 2D\delta(t')$, and $U(x,t)$ is the quad-stable generalized potential function and $U_0(x)$ is the system potential function as follows:

$$\begin{cases} U(x,t) = U_0(x) - x\varepsilon(t), \\ U_0(x) = -\dfrac{a_1^2b_1^2c_1^2}{2}x^2 + \dfrac{a_1^2b_1^2 + b_1^2c_1^2 + c_1^2a_1^2}{4}x^4 \\ \qquad\quad - \dfrac{a_1^2 + b_1^2 + c_1^2}{6}x^6 + \dfrac{x^8}{8}, \end{cases} \tag{2}$$

$\varepsilon(t) = A\sin(2\pi ft + \phi_i)$ is the input periodic signal where the phase is usually ignored which can be simplified as $\varepsilon(t) = A\sin(2\pi ft)$. $U_0(x)$ can be expressed by parameter m as shown in Eq. (3):

$$\begin{aligned} U_0(x,m) = {} & \frac{m^3(m^3 - 12m^2 + 44m - 48)}{128}x^2 + \frac{m(m-4)}{8}x^6 \\ & + \frac{m^2(3m^3 - 24m + 44)}{64}x^4 + \frac{1}{8}x^8, \end{aligned} \tag{3}$$

where

$$a_1 = \sqrt{-m(m-2)}/2, \quad b_1 = \sqrt{-m(m-4)}/2,$$
$$c_1 = \sqrt{-m(m-6)}/2.$$

$U_0(x)$ has four steady-state points:

$$s_1 = -\sqrt{-m(m-6)}/2, \quad s_2 = -\sqrt{-m(m-2)}/2,$$
$$s_3 = \sqrt{-m(m-2)}/2, \quad s_4 = \sqrt{-m(m-6)}/2$$

and three unstable points: $s_5 = \sqrt{-m(m-4)}/2$, $s_0 = 0$, $s_6 = -\sqrt{-m(m-4)}/2$.

Figures 1(a) and 1(b) are the potential function of $U_0(x)$ and $U_1(x)$, respectively. By adjusting m, it can be found that it is a quad-stable state when $0 < m \le 2$, a tri-stable state when $2 < m \le 4$ and a bistable state when $4 < m \le 6$.

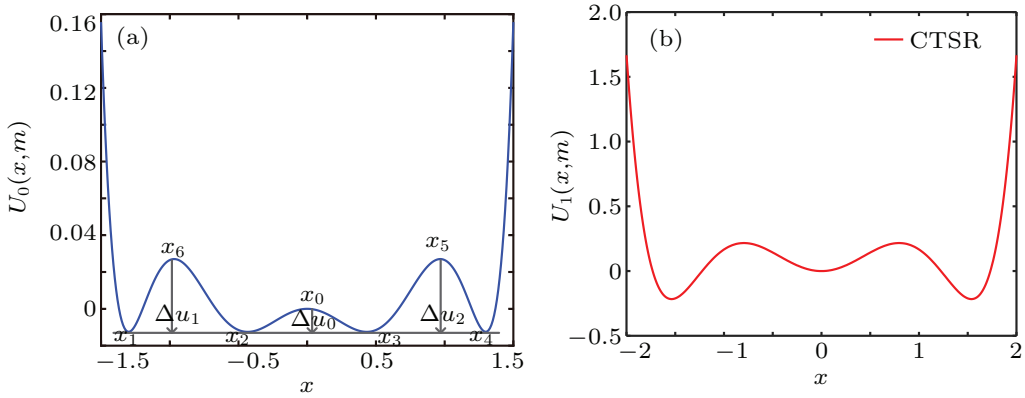


Fig. 1. Potential functions of $U_0(x,m)$ and $U_1(x)$: (a) $U_0(x,m)$ of QSR ($m = 1.5$), (b) $U_1(x)$ of CTSR ($a = 1.5$, $b = 3$, and $c = 1$).

Figure 2 is the potential function of QSR with m. It can be seen that the potential well of $U_0(x,m)$ on both sides shifts to the right and the well depth changes as m increases, while the middle potential well changes insignificantly.

Figure 3(a) shows the variation of the potential well force, which is symmetric about the origin and fluctuates between $(-0.5, 0.5)$. It can be concluded that the nonlinear forces play an essential role on the shape of potential force. Figure 3(b) shows the height of the potential barriers. When m is less than m_c, all barriers' height is increasing, and the middle one is higher than the others, which indicates that the particles need more energy to transit from the middle wells to the outer wells. In contrast when m is higher or equal than m_c, the particle needs less energy. The height of the middle barrier is $\Delta u_0 = m^4(m^2 - 8m + 12)^2/2048$, and $\Delta u_1 = \Delta u_2 = m^4/128$ for the other barriers.

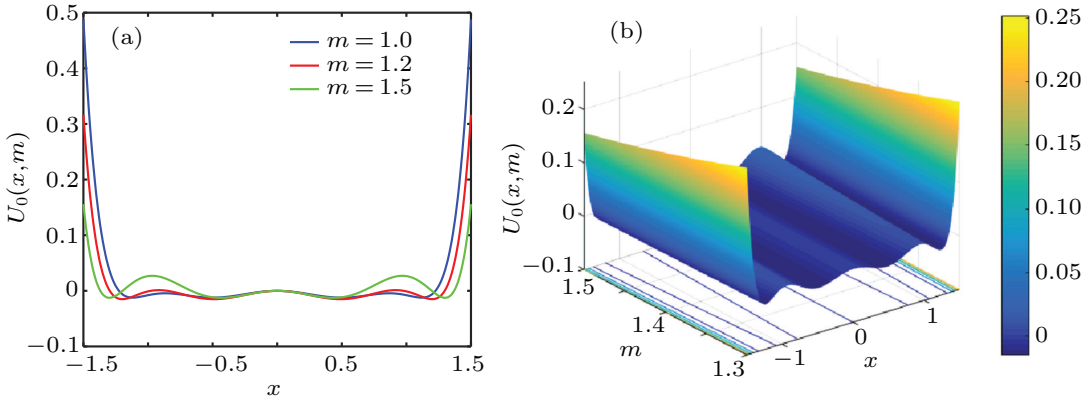


Fig. 2. $U_0(x,m)$ varies with m and x: (a) $U_0(x,m)$ varies with m and x, (b) $U_0(x,m)$ varies with m and x.

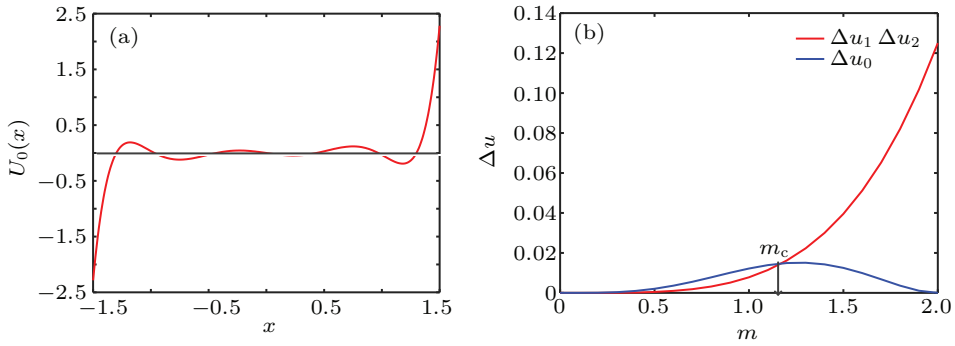


Fig. 3. Potential well force and potential barrier: (a) potential well force, (b) potential barrier.

2.2. SPD of QSR

From Eq. (1), the corresponding FPE is:

$$\frac{\partial \rho}{\partial t} = -\frac{\partial}{\partial x}\left[\left(-\frac{\partial U_0(x,m)}{\partial x} + A\sin(2\pi f t)\right)\rho\right] + D\frac{\partial^2 \rho}{\partial x^2}, \quad (4)$$

where ρ is the probability density function, $\partial\rho/\partial t$ consists of the drag term and the diffusion term on the right. According to the adiabatic approximation theory, SPD[40] is given by

$$\rho_{\rm st} = N\exp\left[-\frac{U(x,t)}{D}\right], \quad (5)$$

where N is a normalized constant $N = [\int \mathrm{e}^{-U(x,t)/D}\mathrm{d}x]^{-1}$, and $U(x,t)$ is a generalized function, as shown in Eq. (2).

Setting $A = 0$, figure 4 shows the impacts of m and D on SPD. Studying the relationship between $\rho_{\rm st}$ and each parameter facilitates the analysis of the particle motion state. Therefore, by keeping m fixed and increasing D, the overall trend in the potential wells on both sides and the middle potential well remains unchanged. But the peak value is smaller, indicating that the particle transition requires less energy. When D is constant, the depth of the outer potential wells getting deeper and that of the inner well is shallower as m increases, indicating that the particles are easier to transit from the inner potential wells to the outer wells.

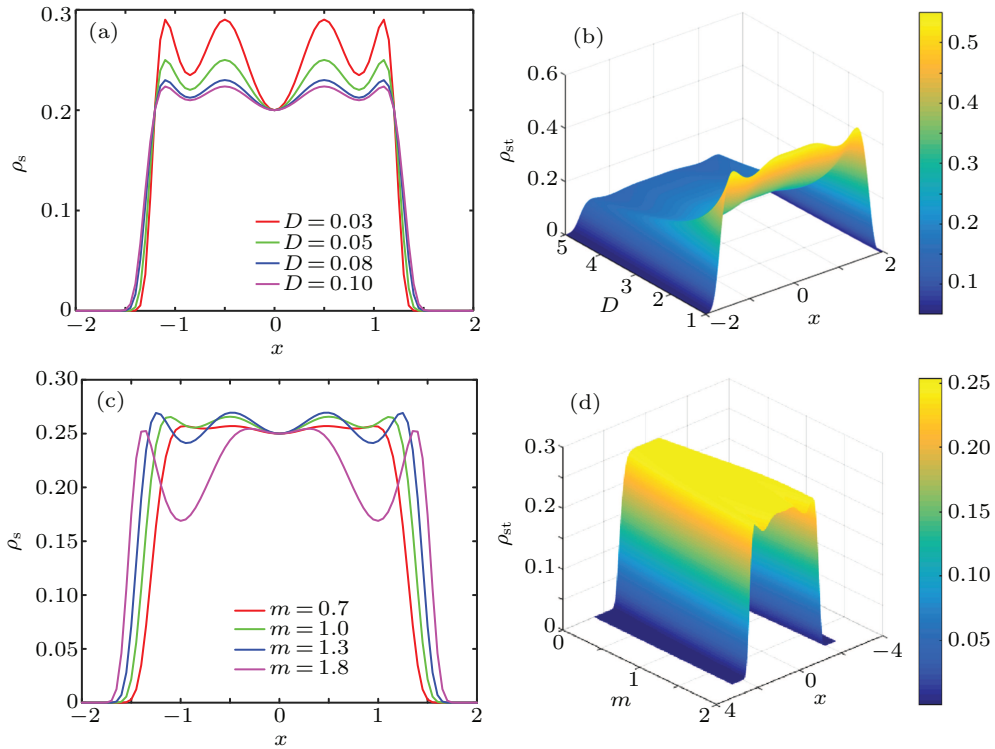


Fig. 4. $\rho_{\rm st}$ varies with D, m, and x: (a) $\rho_{\rm st}$ varies with D and x ($m = 0.95$), (b) $\rho_{\rm st}$ varies with D and x ($m = 0.95$), (c) $\rho_{\rm st}$ varies with m and x ($D = 0.2$), (d) $\rho_{\rm st}$ varies with m and x ($D = 0.2$).

2.3. MFPT of QSR

Assuming that the probability between each steady state satisfies $\sum_{n=1}^{4} p_n(t) = 1$, and the initial transition rate satisfies $K^{(0)}(t) = (\sqrt{U''_{(\rm un)}U''_{(\rm st)}}/2\pi)\exp(-\Delta U/D)$:

$$\begin{cases} K_{43}^{(0)} = K_{12}^{(0)} = \dfrac{\sqrt{|U''(x_5)U''(x_4)|}}{2\pi} \exp\left(-\dfrac{U(x_5)-U(x_4)}{D}\right), \\ K_{34}^{(0)} = K_{21}^{(0)} = \dfrac{\sqrt{|U''(x_3)U''(x_5)|}}{2\pi} \exp\left(-\dfrac{U(x_5)-U(x_3)}{D}\right), \\ K_{32}^{(0)} = K_{23}^{(0)} = \dfrac{\sqrt{|U''(x_0)U''(x_3)|}}{2\pi} \exp\left(-\dfrac{U(x_0)-U(x_3)}{D}\right). \end{cases} \tag{6}$$

The corresponding kinetic equation is:

$$\frac{\mathrm{d}P_i}{\mathrm{d}t} = \sum_{j=1}^{n} Q_{ij}(t)P_j, \quad i = 1,2,3, \ j = 1,2. \tag{7}$$

The main equation can be obtained as:

$$\begin{cases} \dfrac{\mathrm{d}P_1}{\mathrm{d}t} = P_2K_{21} - P_1K_{12}, \\ \dfrac{\mathrm{d}P_2}{\mathrm{d}t} = P_1K_{12} + P_3K_{32} - P_2K_{21} - P_2K_{23}, \\ \dfrac{\mathrm{d}P_3}{\mathrm{d}t} = P_4K_{43} + P_2K_{32} - P_3K_{32} - P_3K_{34}, \\ \dfrac{\mathrm{d}P_4}{\mathrm{d}t} = P_3K_{34} - P_4K_{43}. \end{cases} \tag{8}$$

The corresponding transfer operator Q is:

$$Q = \begin{bmatrix} -K_{12} & K_{21} & 0 & 0 \\ K_{12} & -K_{21}-K_{23} & K_{32} & 0 \\ 0 & K_{23} & -K_{32}-K_{34} & K_{34} \\ 0 & 0 & -K_{12} & -K_{12} \end{bmatrix}, \tag{9}$$

$K_{i,i+1}(t) = K_{i,i+1}^{(0)}(t)\exp\left(\frac{\varepsilon(t)}{D}\Delta x_{i,i+1}\right)$, which can be expanded by Taylor's equation to $K_{i,i+1}(t) = K_{i,i+1}^{(0)}(t) \pm \varepsilon(t)\Delta_{i,i+1}$, $\Delta_{i,i+1} = K_{i,i+1}^{(0)}\Delta x_{i,i+1}/D$, namely:

$$\begin{cases} K_{12}(t) = K_{43}(t) = K_{12}^{(0)}(t) \mp K_{12}^{(0)}(t)\exp\left(\dfrac{(x_5-x_4)\varepsilon(t)}{D}\right), \\ K_{21}(t) = K_{34}(t) = K_{21}^{(0)}(t) \mp K_{21}^{(0)}(t)\exp\left(\dfrac{(x_5-x_3)\varepsilon(t)}{D}\right), \\ K_{32}(t) = K_{23}(t) = K_{32}^{(0)}(t) \mp K_{32}^{(0)}(t)\exp\left(\dfrac{x_2\varepsilon(t)}{D}\right). \end{cases} \tag{10}$$

MFPT from potential well x_i to x_j can be obtained through the transition probability of Eq. (10), namely $T_{ij} = K_{ij}^{-1}(t)$.

Figures 5–7 show changes of MFPT with m and D. Fixing D and increasing m, when $m < 1$, T_{12} increases with increasing D, when $m \geq 1$, T_{12} decreases with increasing D. The smaller T_{12}, the greater the probability of particle transition, which indicates easier particle transition and stronger SR characteristics. T_{43} shows the same characteristics as T_{12}. In the same way, T_{34} and T_{23} both decrease monotonously with the increase of D and the escape rate of particles increases. Fixing D and increasing m, T_{34} and T_{23} decrease. T_{21} has the same characteristics as T_{34}, T_{32} has the same characteristics as T_{23}. The above results show that the escape rate of the particle is greater as m and D increase, which indicates stronger SR characteristics.

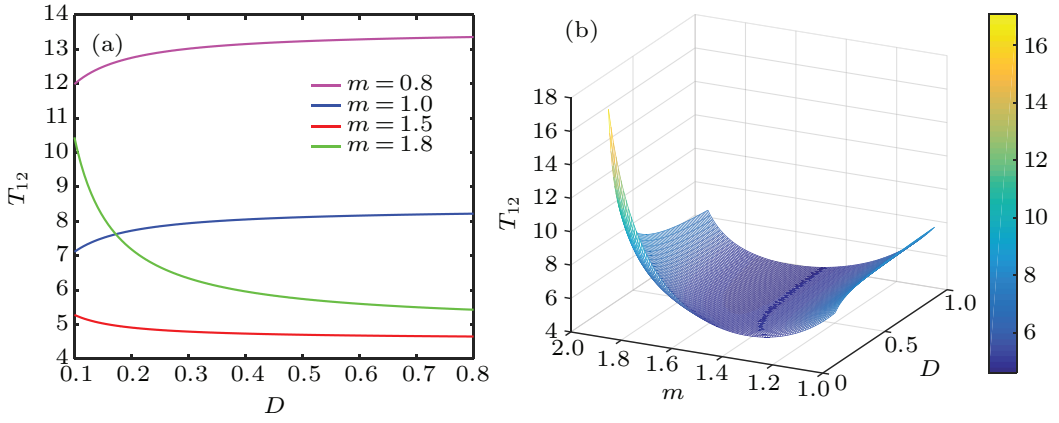


Fig. 5. T_{12} or T_{43} varies with D and m: (a) T_{12} or T_{43} varies with D and m, (b) T_{12} or T_{43} varies with D and m.

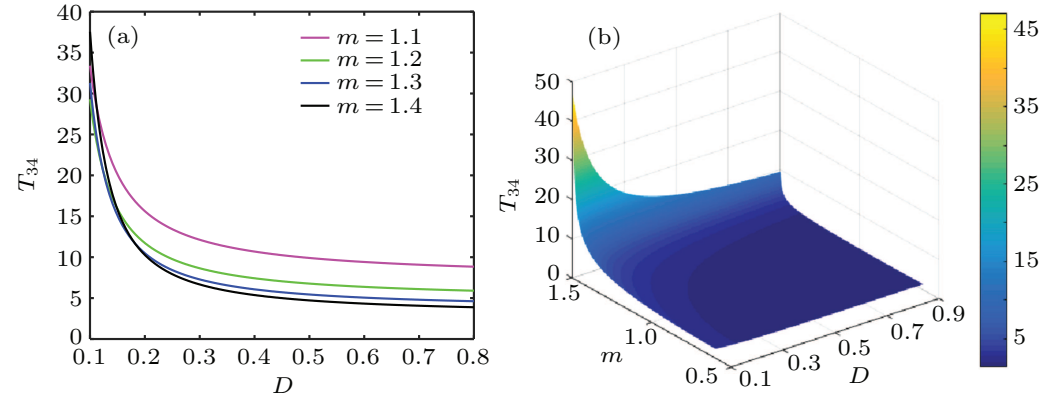


Fig. 6. T_{34} or T_{21} varies with D and m: (a) T_{34} or T_{21} varies with D and m, (b) T_{34} or T_{21} varies with D and m.

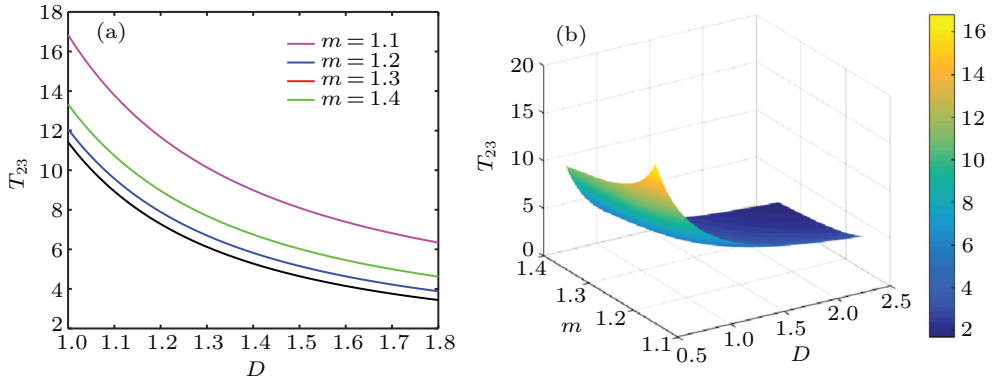


Fig. 7. T_{23} or T_{32} varies with D and m: (a) T_{23} or T_{32} varies with D and m, (b) T_{23} or T_{32} varies with D and m.

2.4. *W* of QSR

From Eq. (7), $P=(P_1,P_2,P_3,P_4)$ can be expanded as $P(t)=P_i^{(0)}+A\Delta P(t)$. Combining $P(t)=P_i^{(0)}+A\Delta P(t)$ and Eq. (10), it can be shown as[41]

$$\begin{aligned} P_1^{(0)} &= P_4^{(0)} = K_{21}^{(0)}/2K_{21}^{(0)}+K_{43}^{(0)}, \\ P_3^{(0)} &= P_2^{(0)} = K_{43}^{(0)}/2K_{21}^{(0)}+K_{43}^{(0)}. \end{aligned} \tag{11}$$

Then, $P=(P_1,P_2,P_3,P_4)$ can be obtained as:

$$\begin{cases} P_1 = P_1^{(0)} - K_{34}^{(0)}(x_5-x_3)/4K_{12}^{(0)}((4Q_9/x_5-x_4)+4(Q_{10}+Q_{11})+Q_{12}), \\ P_2 = P_2^{(0)} + Q_7(P_3^{(0)}-Q_5-1/4)-Q_9+(Q_{10}+Q_{11})(x_4-x_5), \\ P_3 = P_3^{(0)} + Q_7(P_3^{(0)}-Q_5-1/4)-Q_9+(Q_{10}+Q_{11})(x_4-x_5), \\ P_4 = P_4^{(0)} + K_{34}^{(0)}(x_5-x_3)/4K_{12}^{(0)}((4Q_9/x_5-x_4)+4(Q_{10}+Q_{11})+Q_{12}), \end{cases} \tag{12}$$

$$\begin{aligned} Q_1 &= 2\pi f(x_5-x_4), \\ Q_2 &= 2K_{32}^{(0)}(x_4-x_5)+K_{34}^{(0)}(x_4-x_3), \\ Q_3 &= 2\pi f(K_{12}^{(0)}(x_4-x_5)+K_{34}^{(0)}(x_3-x_5)), \\ Q_4 &= 2K_{12}^{(0)}K_{32}^{(0)}(x_3-x_6), \\ Q_5 &= 2A\pi f P_3^{(0)}(x_4-x_5)^2 \\ &\quad \times(2K_{32}^{(0)}x_2+K_{34}^{(0)}(x_3-x_4))/D(Q_4^2+Q_5^2), \\ Q_6 &= AP_3^{(0)}(K_{34}^{(0)}x_4-x_3(K_{34}^{(0)}+2K_{32}^{(0)})), \\ Q_7 &= \exp((2K_{32}^{(0)}(x_5-x_4)+K_{34}^{(0)}(x_3-x_4))t/(x_4-x_5)), \\ Q_8 &= \exp(2tK_{12}^{(0)}K_{32}^{(0)}(x_5-x_4)/K_{12}^{(0)}(x_4-x_5) \\ &\quad +K_{34}^{(0)}(x_3-x_5)), \\ Q_9 &= Q_8(P_3^{(0)}-1/4-AQ_3Q_4x_3P_3^{(0)}/D(Q_3^2+Q_4^2)), \\ Q_{10} &= Q_6(Q_1\cos(2\pi ft)+Q_2(\varepsilon(t)/A))/D(Q_1^2+Q_2^2), \\ Q_{11} &= 2x_3AP_3^{(0)}K_{12}^{(0)}K_{32}^{(0)}(Q_4(\varepsilon(t)/A) \\ &\quad -Q_3\cos(2\pi ft))/D(Q_3^2+Q_4^2), \\ Q_{12} &= Q_7(4P_3^{(0)}-4Q_5-1)/(x_4-x_5). \end{aligned}$$

The conditional probability is $P(x,t)=P_4\Delta(x-x_4)+P_5\Delta(x-x_5)+P_3\Delta(x-x_3)+P_2\Delta(x-x_2)$, then the corresponding average asymptotic response $\langle x(t)\rangle$ is

$$\langle x(t)\rangle = \int xP(x,t)\,\mathrm{d}x = x_4(P_4-P_1)+x_3(P_3-P_2). \tag{13}$$

Equation (1) is multiplied by $\mathrm{d}x$ on both sides to obtain:

$$\begin{aligned} \frac{\mathrm{d}U_0(x)}{\mathrm{d}t}\mathrm{d}x &= \mathrm{d}\left(\frac{U_0^2(x)}{2}\right) \\ &= \left[-\frac{\mathrm{d}x}{\mathrm{d}t}-\frac{\mathrm{d}U_0(x)}{\mathrm{d}t}+\varepsilon(t)+\varsigma(t)\right]\mathrm{d}x. \end{aligned} \tag{14}$$

When there is an external force, the expression of its potential function is $U(x,t)=U_0(x)-x\varepsilon(t)$, then differentiation obtains the expression:

$$\begin{aligned} \mathrm{d}U &= \frac{\partial U}{\partial x}\mathrm{d}x+\frac{\partial U}{\partial t}\mathrm{d}t \\ &= \left(\frac{\partial U_0}{\partial x}-\varepsilon(t)\right)\mathrm{d}x-x\frac{\partial \varepsilon(t)}{\partial t}\mathrm{d}t. \end{aligned} \tag{15}$$

The work which periodic signals do on the system is: $\mathrm{d}W=\int -2\pi A\cos(2\pi ft)\,\mathrm{d}t$. By averaging the external force of the signal in each period, W can be obtained as:

$$W=\int \mathrm{d}W = \frac{1}{N}\left(\int_{t_1}^{t_1+N/f} -2A\pi f\cos(2\pi ft)\,\langle x(t)\rangle\,\mathrm{d}t\right). \tag{16}$$

Figure 8 shows the relationship between $\langle x(t)\rangle$ and D. When $A=0.0025$, $f=0.001$, $N=300$, $\langle x(t)\rangle$ varies periodically with D, indicating that the particles vibrate with larger D and the transition time.

Figure 9 shows the change of W with D and m, W first increases and then decreases as D increases. By fixing D and increasing m, W shows a single peak. By adjusting m, the single peak can be converted to the double peak, but the peak value is reduced. This is because the QSR have the double quad-stable's characteristics when $0<m\leq 2$, which is consistent with the theory.

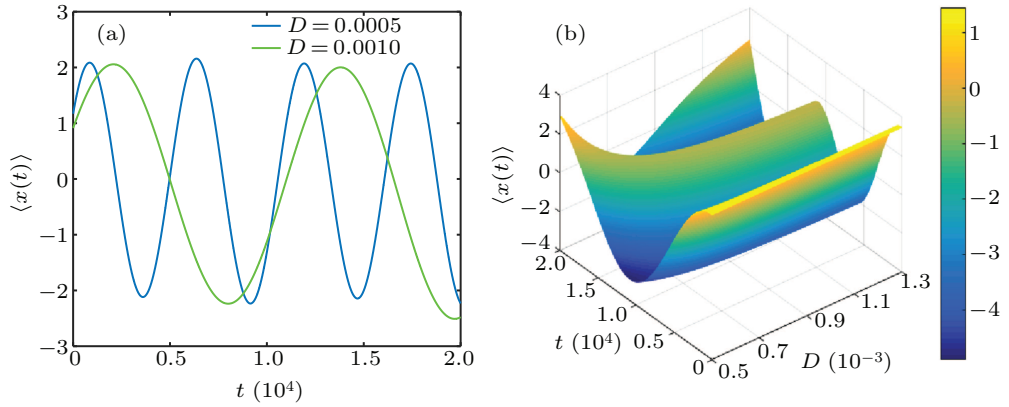


Fig. 8. $\langle x(t)\rangle$ varies with D and t: (a) $\langle x(t)\rangle$ varies with D and t ($m = 0.6$), (b) $\langle x(t)\rangle$ varies with D and t ($m = 0.6$).

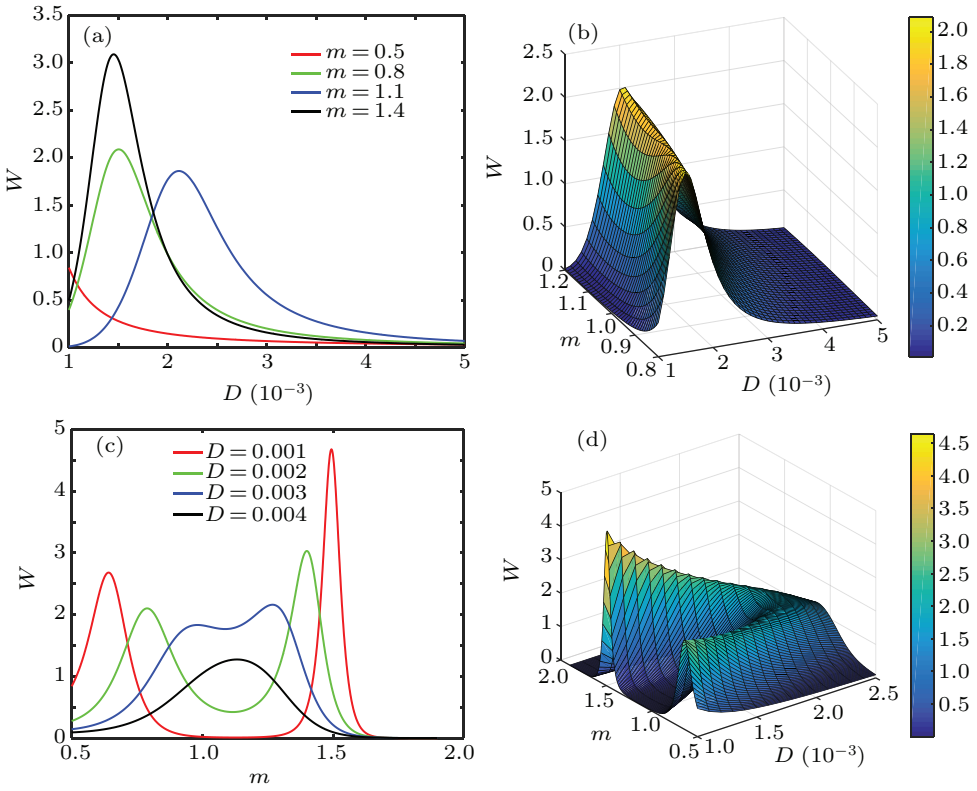


Fig. 9. W varies with D and m: (a) W varies with m, (b) single peak, (c) W varies with D, (d) double peak.

2.5. SAF of QSR

By simplifying the conditional probability and Eq. (13)

$$\begin{cases} P_i(t) = H_i\varepsilon(t) \quad \phi_i = \arctan\left(\dfrac{C_i}{D_i}\right), \\ H_i = A\sqrt{C_i^2 + D_i^2}, \end{cases} \tag{17}$$

$C_i = -\omega(K_0^2 + \omega^2 I)^{-1}\Delta P_0$, $D_i = -K_0(K_0^2 + \omega^2 I)^{-1}\Delta P_0$ and then represented by the eigenvalue λ_k, β_k

$$\begin{cases} K_0\lambda_k = \lambda_k\beta_k \\ \Delta P_0 = \sum\limits_{k=1}^{4}\lambda_k\gamma_k, \end{cases} \rightarrow \begin{cases} C_i = -\sum\limits_{i=1}^{4}\dfrac{\omega}{\beta_k^2 + \omega^2}\lambda_k\gamma_k \\ D_i = -\sum\limits_{i=1}^{4}\dfrac{\lambda_k}{\beta_k^2 + \omega^2}\lambda_k\gamma_k. \end{cases} \tag{18}$$

Under the limitation of a long time, the output power of $\langle x(t)\rangle^2$ is

$$E = G_1^2 + G_2^2 + 2G_1G_2\sin(\theta_1 - \theta_2), \tag{19}$$

$$\theta_1 = \arctan\left(\left(\frac{x_1H_1 - x_2H_2}{x_1H_1 + x_2H_2}\right)\tan(\phi_1 - \phi_2/2)\right),$$
$$\theta_2 = \arctan\left(\left(\frac{x_3H_3 - x_4H_4}{x_3H_3 + x_4H_4}\right)\tan(\phi_3 - \phi_4/2)\right),$$
$$G_1 = \sqrt{x_1^2H_1^2 + x_2^2H_2^2 + 2x_1H_1x_2H_2\sin(\phi_1 - \phi_2)},$$
$$G_2 = \sqrt{x_3^2H_3^2 + x_4^2H_4^2 + 2x_3H_3x_4H_4\sin(\phi_3 - \phi_4)}.$$

So SAF[41,42] can be expressed as

$$\mathrm{SAF} = E/A^2. \tag{20}$$

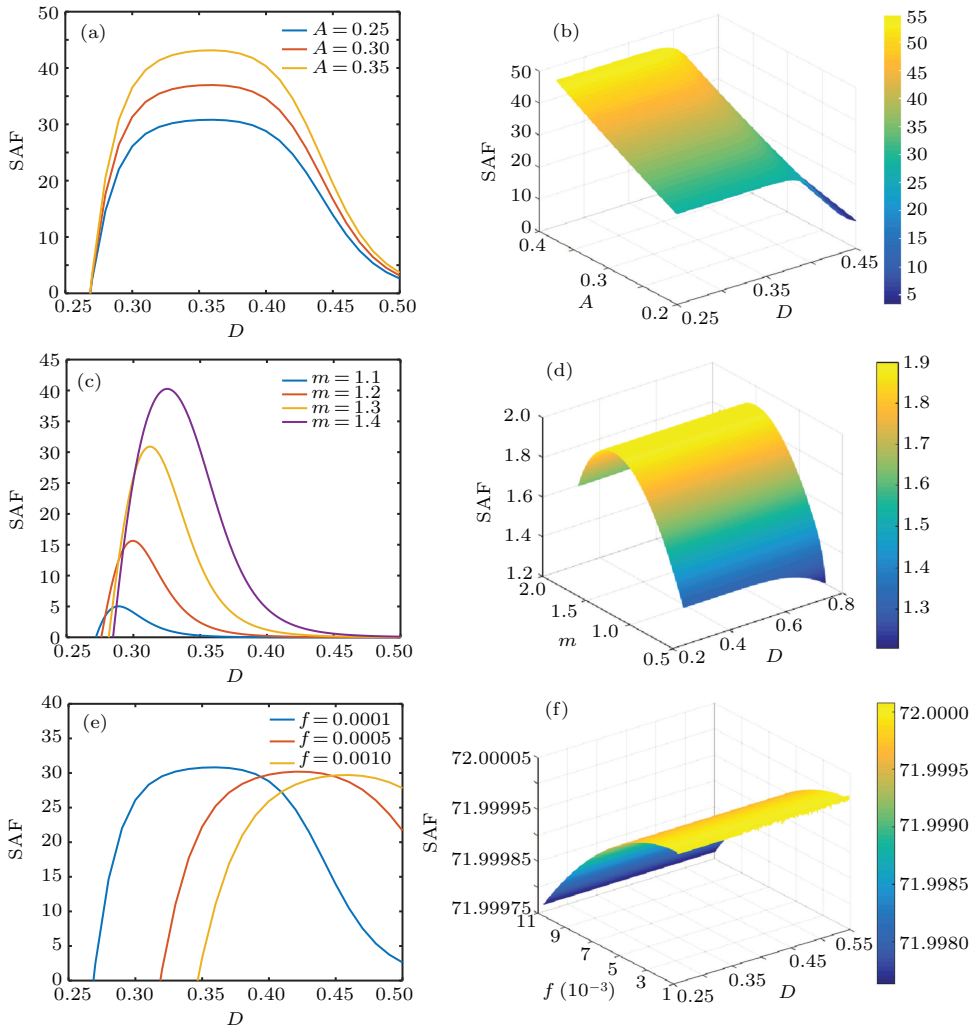


Fig. 10. Variation of SAF with A, m, f: (a) SAF varies with D and A ($m = 1.5$), (b) SAF varies with D and A ($m = 1.5$), (c) SAF varies with D and m, (d) SAF varies with D and m, (e) SAF varies with D and f ($m = 1.2$), (f) SAF varies with D and f ($m = 1.2$).

Figure 10 shows the effects of A, m, and f on SAF, it can be seen that SAF increases first and then decreases. In Fig. 10(a) and Fig. 10(b), when other parameters remain fixed, SAF is proportional to A and m and the peak increases with the increase of A and m, respectively. In Fig. 10(c), SAF is steeper than that in Fig. 10(a), indicating that m is more sensitive to SAF than A. In Fig. 10(e) and Fig. 10(f), f has little effect on the peak of SAF, which is inversely proportional to f, and the peak shifts to right where D is bigger as f increase.

3. Numerical simulation and engineering application

To verify the rules of the above theoretical analysis, GA and the fourth-order Runge–Kutta algorithm are combined to perform numerical simulations to obtain the optimal parameters: $m = 0.956$, $a = 1.5125$, $b = 3.0301$, $c = 1.0185$. In Fig. 11, the noise signal is processed by QSR with a stronger periodicity and a higher amplitude, which is about 40 times than CTSR at low frequency conditions ($f = 0.1$Hz). The frequency band of the noise is also shifted by QSR.

In Fig. 12, the original signal's spectral amplitude is 75.49 before any processing. Then it is processed by QSR to obtain more periodicity and greater amplitude which is 539.7 and is 4 times that of CTSR and 7 times that of the original signal at high frequency conditions ($f = 25$ Hz). The results show that the amplification performance of QSR is higher than CTSR in low frequency and high frequency conditions.

Figures 11 and 12 show the time domain and frequency domain figures of the low and the high-frequency signal, setting the frequency of the periodic signal to 0.01 Hz and 25 Hz respectively. To verify that QSR has superior amplitude amplification and periodicity than CTSR not only at low frequencies and at high frequencies, but also at multi-frequencies. Then the periodic signal is added: $\varepsilon(t) = 0.1\sin(2\pi \times 0.05t) + 0.3\sin(2\pi \times 0.03t) + 0.5\sin(2\pi \times 0.01t)$. Obviously, from Fig. 13 the amplitude are 2.6 times, 1.1 times and 1.83 times that of the original multi-frequency signal amplitude, respectively, at 0.01 Hz, 0.03 Hz, and 0.05 Hz after CTSR processing. The amplitude are 6.9 times, 2.08 times, and 3.27 times that of the original multi-frequency signal amplitude after QSR processing. It can be seen that the amplification capability is stronger and the periodicity is better after QSR under high frequency and multi-frequency.

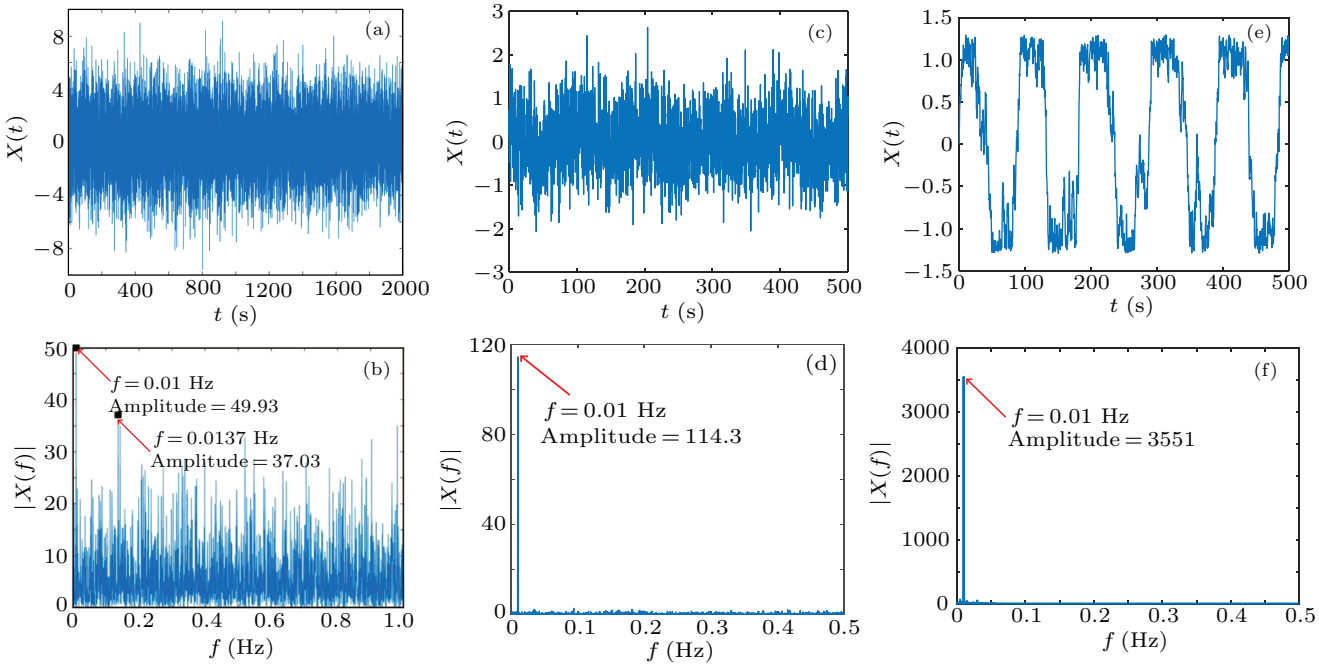


Fig. 11. Compare the time and frequency domains of two systems at low frequencies (0.01 Hz): (a) time domain diagram of input noise, (b) frequency domain diagram of input signal, (c) time-domain diagram with noise of CTSR, (d) frequency domain diagram with noise of CTSR, (e) time-domain diagram with noise of QSR, (f) frequency domain diagram with noise of QSR.

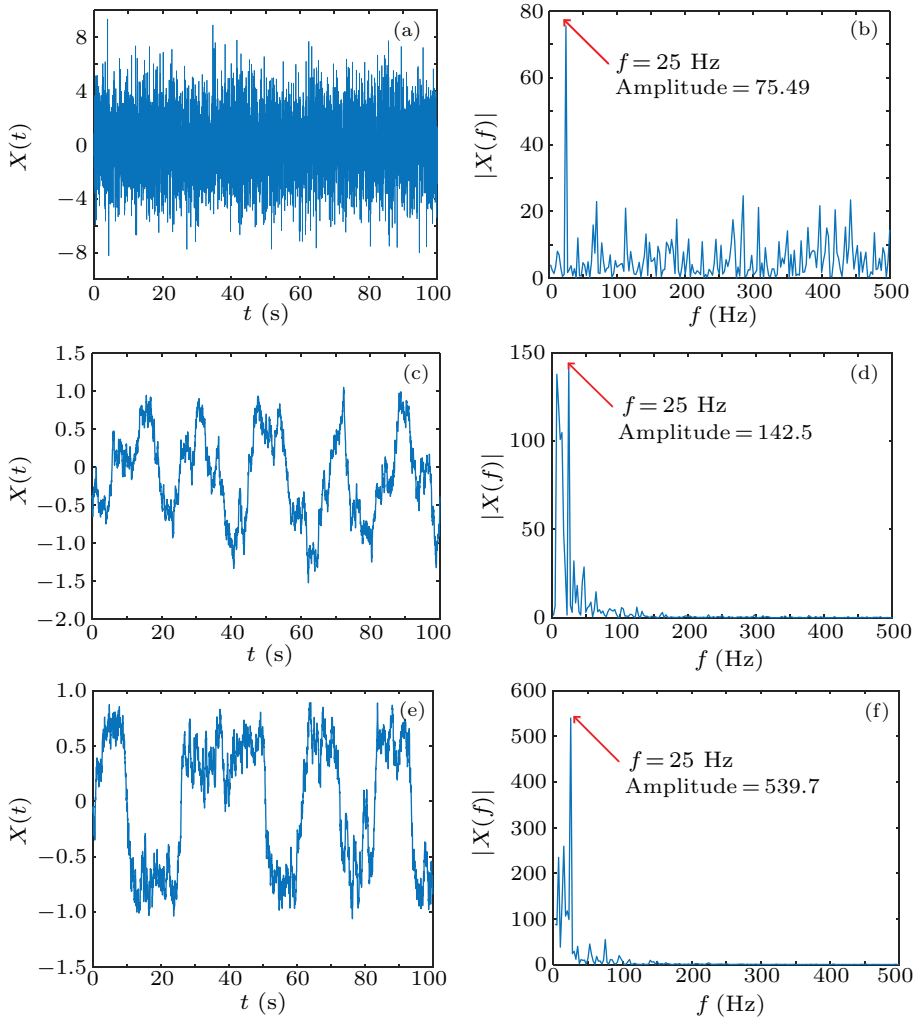


Fig. 12. Comparison of the time and frequency domains of two systems at high frequencies (25 Hz): (a) time domain diagram of input noise, (b) frequency domain diagram of input signal, (c) time-domain diagram with noise of CTSR, (d) frequency domain diagram with noise of CTSR, (e) time-domain diagram with noise of QSR, (f) frequency domain diagram with noise of QSR.

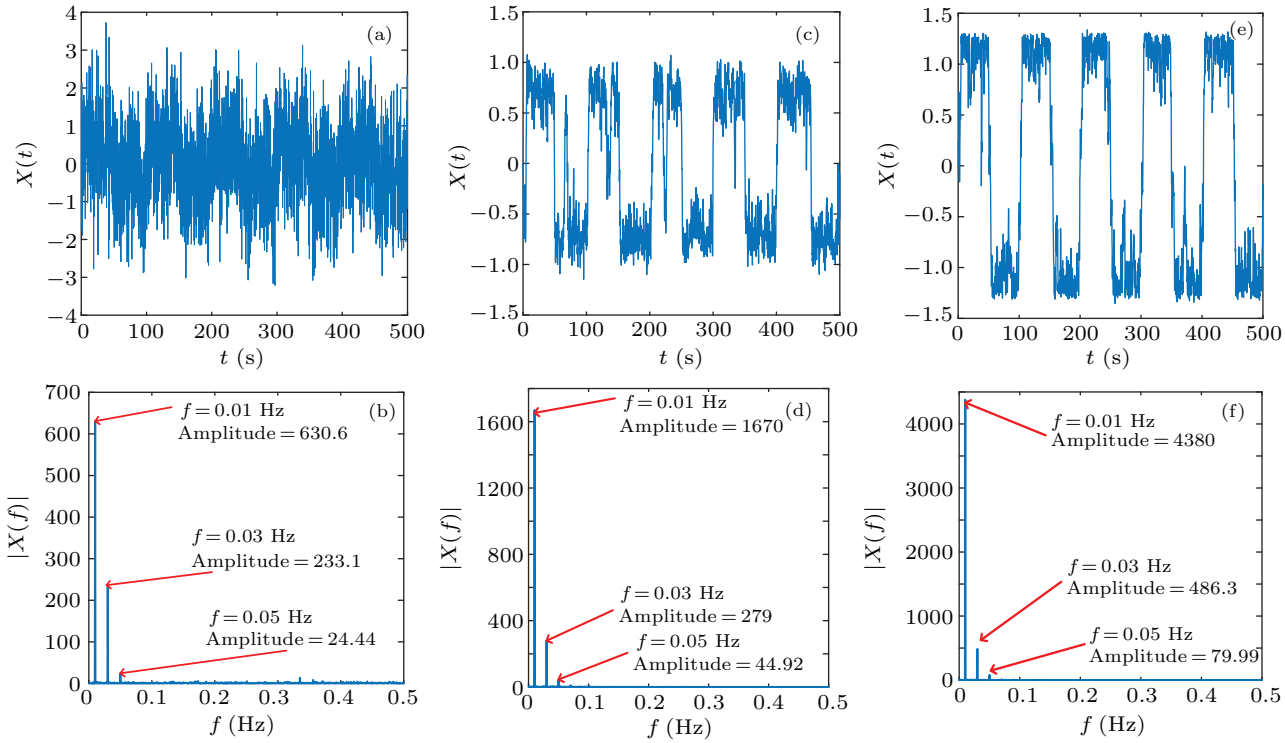


Fig. 13. Comparison of the time and frequency domains of two systems at multi-frequency: (a) time domain diagram of input noise, (b) frequency domain diagram of input signal, (c) time-domain diagram with noise of CTSR, (d) frequency domain diagram with noise of CTSR, (e) time-domain diagram with noise of QSR, (f) frequency domain diagram with noise of QSR.

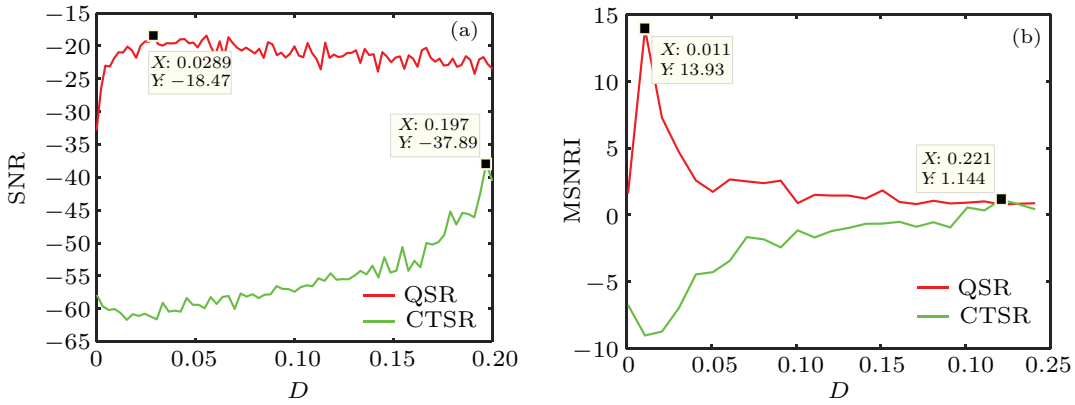


Fig. 14. Comparison of SNR and MSNRI: (a) comparison of SNR ($m = 0.2$, $a = 1.8$, $b = 3$, $c = 1$), (b) comparison of MSNRI ($m = 1.5$, $a = 1.8$, $b = 3$, $c = 1$).

In Fig. 14, SNR of QSR is about 2 times and MSNRI is about 12 times than CTSR, where the peak of SNR in QSR and CTSR is −18.47 dB and −37.89 dB, respectively. The peak of MSNRI in QSR and CTSR is 13.93 dB and 1.144 dB, respectively, which shows that SNR of QSR is improved by 19.42 dB relative to CTSR. This indicates QSR is superior in noise immunity.

4. Bearing fault detection and application

4.1. 6205-2RS JEM SKF bearing fault detection

To verify the feasibility of QSR in practical engineering applications under different scenarios, the performance of QSR and CTSR for detecting faults is compared in this section. Due to the small public data set of actual bearing faults, the data from Case Western Reserve University (CWRU), model 6205-2RS JEM SKF[41] is widely used by domestic and international scholars. The experimental rig is shown in Fig. 15.

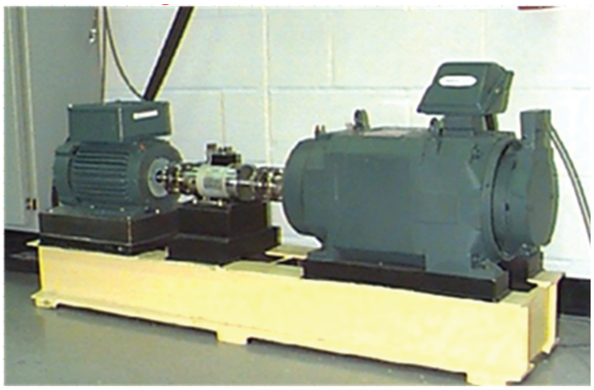


Fig. 15. 6205-2RS JEM SKF deep groove ball bearing test device.

(i) Inner ring fault detection

Figures 16(a) and 16(b) show the time–frequency diagrams of the bearing inner ring fault signal, and the characteristic frequency of the fault signal cannot be identified. Figures 16(c)–16(f) are the time–frequency diagram of the output signals of CTSR and QSR. Due to the limitation of small parameters, secondary sampling is used for pre-processing, and the sampling frequency is $f_{sr} = 5$ Hz. Then, the optimal parameters of the two systems can be obtained by GA, the optimal parameters of CTSR and QSR are: $a = 1.2154$, b =2.5492, $c = 1.01596$, and $m = 1.38641$. From Fig. 16(c), Fig. 16(d), Fig. 16(e), and Fig. 16(f), it can be seen that the frequency domain diagrams of the two systems show peaks at $f = 162$ Hz (relative error is 0.123%). At this time, the SNR of QSR and CTSR are −3.7363 dB and −2.8159 dB respectively, which is an improvement of 0.9204 dB. QSR has a larger peak and less noise interference than CTSR, which makes easier to detect the inner ring fault and indicates the superiority of QSR.

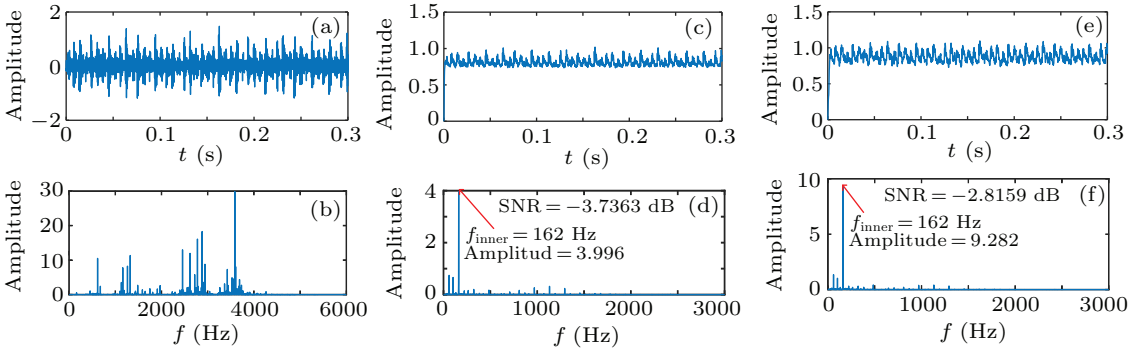


Fig. 16. Inner ring fault detection of CTSR and QSR: (a) Time domain of inner ring fault signal, (b) frequency domain of inner ring fault signal, (c) inner ring fault detection time domain of CTSR, (d) inner ring fault detection frequency domain of CTSR, (e) inner ring fault detection time domain of QSR, (f) inner ring fault detection frequency domain of QSR.

(ii) Outer ring fault detection

Figures 17(a) and 17(b) show the time–frequency diagrams of the bearing outer ring fault signal. It can be seen that the fault signal is completely submerged in noise and the characteristic frequency of the fault signal cannot be identified. QSR and CTSR are used to detect the fault signal. Then, the optimal parameters of the two systems can be obtained by GA. The optimal parameters of CTSR are: $a = 1.0028$, b =2.16974, $c = 1.0095$, and the optimal parameter of QSR is: $m = 1.09348$. Comparing Fig. 17(c), Fig. 17(d), Fig. 17(e), and Fig. 17(f), it can be seen that the frequency domain diagrams of both systems show peaks at $f = 108$ Hz (the relative error is 0.65%), which indicates that the characteristic frequency of the fault signal is detected. Figures 17(e) and 17(f) are the output signal of QSR, it can be seen that the time domain signal exhibits periodicity and the peak of the spectrum at $f = 108$ Hz is nearly 2 times higher than CTSR. At this time, the SNR of QSR and CTSR is −38.4624 dB and −36.6194 dB, respectively, which is an improvement of 1.842 dB compared with CTSR. The results indicate that QSR has a better detection performance than CTSR.

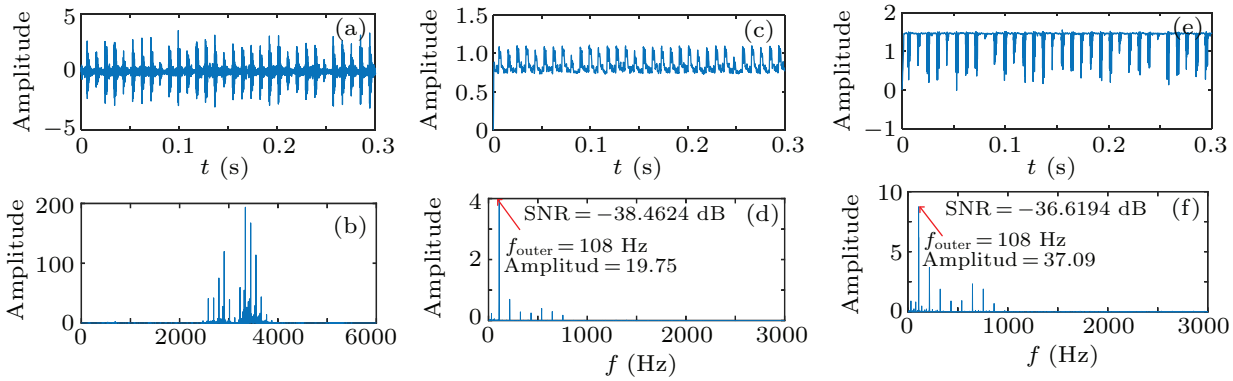


Fig. 17. Outer ring fault detection of CTSR and QSR: (a) time domain of outer ring fault signal, (b) frequency domain of outer ring fault signal, (c) outer ring fault detection time domain of CTSR, (d) outer ring fault detection frequency domain of CTSR, (e) outer ring fault detection time domain of QSR, (f) outer ring fault detection frequency domain of QSR.

4.2. HRB 6205-2Z bearing fault detection

To demonstrate the availability of QSR in different scenarios, another fault data model HRB 6205-2Z is selected for fault detection. The main parameters[43] are shown in Table 1, the experimental station of HRB 6205-2Z in Fig. 18. The sampling frequency is 20 kHz, according to Eq. (21), the inner raceway frequency and outer raceway frequency of the bearing can be obtained theoretically as 117.14 Hz and 78.13 Hz respectively. The proportional compression rate and the secondary sampling frequency are $R = 4000$ and $f_{sr} = f_s/R$=5 Hz, the calculation step is h=1/f_{sr} = 0.2.

$$\begin{cases} f_{\text{inner}} = \dfrac{1}{2} n f_l \left(1 + \dfrac{\mathrm{d}}{D_l} \cos\beta\right), \\ f_{\text{outer}} = \dfrac{1}{2} n f_l \left(1 - \dfrac{\mathrm{d}}{D_l} \cos\beta\right), \end{cases} \tag{21}$$

where n is the number of rolling elements, f_l is rotation frequency, d is diameter of rolling element, D_l is pitch diameter and β is bearing contact angle.

Table 1. The main structure parameters of the tested bearing HRB 6205-2Z.

Bearing Type	Inside diameter (inch)	Outside diameter (inch)	Ball diameter (inch)	Pitch diameter (inch)	Ball number
6205	0.9843	2.0472	0.3126	1.537	9

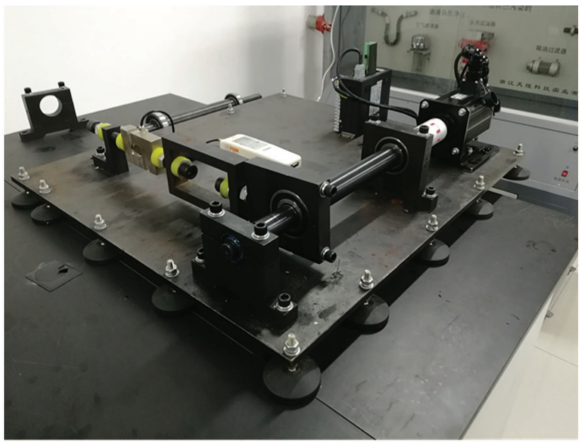


Fig. 18. The experimental station of HRB 6205-2Z.

(i) Inner ring fault detection

The optimal parameters of the two systems can be obtained by GA. The optimal parameters of CTSR and QSR are: $a = 1.3235$, $b = 2.9574$, $c = 1.0028$, $m = 1.4459$. Figures 19(a) and 19(b) show the time–frequency diagrams of the fault signal. It can be seen that the signal is submerged in noise and the characteristic frequency of the fault signal cannot be identified. Figures 19(c)–19(f) are the time–frequency diagrams of the output signals of CTSR and QSR, respectively, in which shows that fault is highlighted at $f = 116$ Hz (the relative error is 0.973%). At this time, the SNR of QSR and CTSR is -29.9642 dB and -31.9351 dB, respectively, which is an improvement of 1.9709 dB. Furthermore, the output signal of QSR has higher spectral peaks and less noise, indicating that QSR has better anti-noise and detection performance.

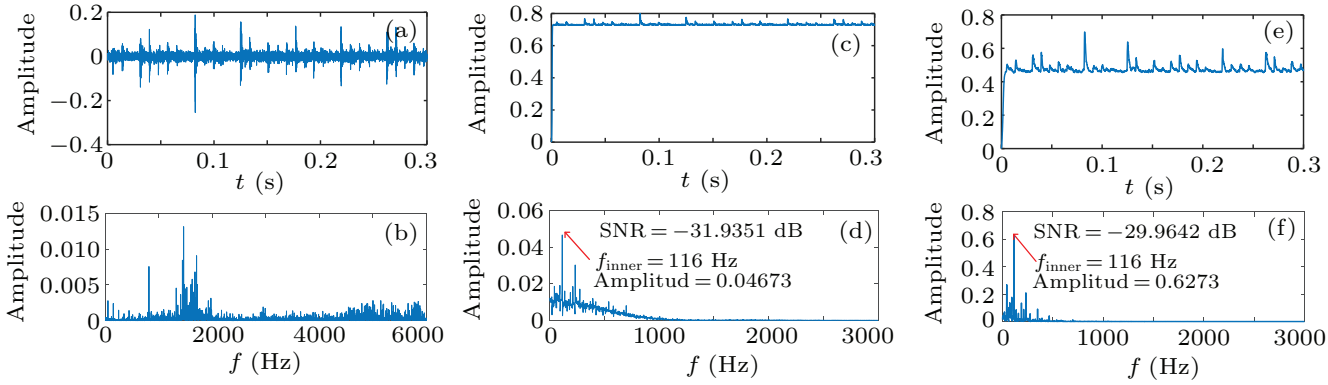


Fig. 19. Inner ring fault detection CTSR and QSR: (a) time domain of inner ring fault signal, (c) inner ring fault detection time domain of CTSR, (b) frequency domain of inner ring fault signal, (d) inner ring fault detection frequency domain of CTSR, (e) inner ring fault detection time domain of QSR, (f) inner ring fault detection frequency domain of QSR.

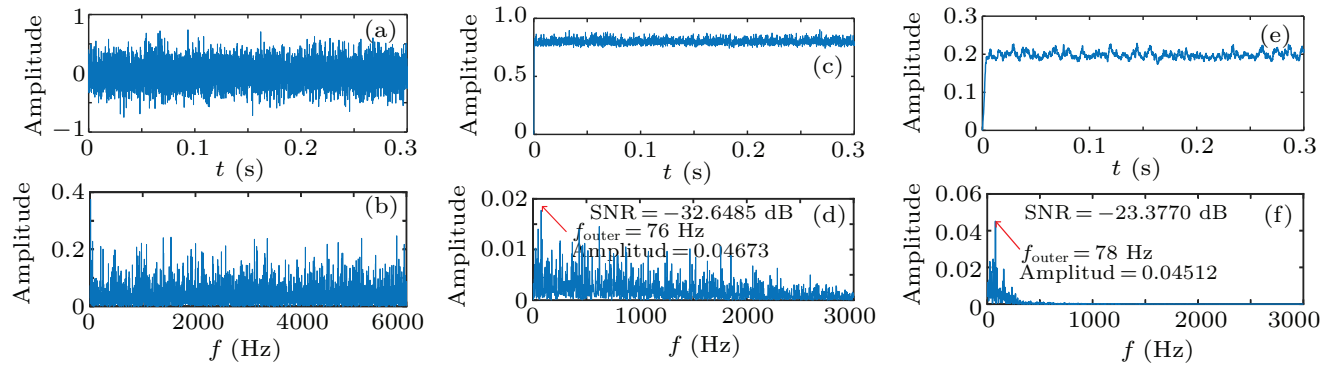


Fig. 20. The outer ring fault detection of CTSR and QSR: (a) time domain of outer ring fault signal, (b) frequency domain of outer ring fault signal, (c) outer ring fault detection time domain of CTSR, (d) outer ring fault detection frequency domain of CTSR, (e) outer ring fault detection time domain of QSR, (f) outer ring fault detection frequency domain of QSR.

(ii) Outer ring fault detection

Similarly, the optimal parameters of the two systems can be obtained by GA. The optimal parameters of CTSR and QSR are: $a = 1.5021$, $b = 3.0121$, $c = 1.1129$, $m = 1.5137$. Figures 20(a) and 20(b) illustrate the time–frequency diagrams of the outer ring fault signal. It can be seen that the signal is submerged in noise and the characteristic frequency of the fault signal cannot be identified. Figures 20(c)–20(f) are the time–frequency diagrams of the output signals of CTSR and QSR. It can be seen that CTSR detected the fault at $f = 76$ Hz (the relative error of 2.731%) and QSR detected the fault at $f = 78$ Hz (the relative error of 0.166%). Apparently, QSR has a lower relative error in fault detection. At this time, the SNR of QSR and CTSR is -23.377 dB and -32.6485 dB, respectively which is an improvement of 9.2715 dB compared with CTSR. The output signal has a higher spectral peak and less noise, indicating that QSR has better noise immunity and detection performance than CTSR.

5. Conclusion and outlook

This paper overcomes the problem of low performance of weak signal enhancement in multi-stable systems and proposes a better QSR. Firstly, the characteristics of MFPT, W, SAF, SNR, and MSNRI are studied and used as the measurement indexes. Then, GA and fourth-order Runge–Kutta algorithm are used to compare the SNR and MSNRI of CTSR and QSR. Finally, CTSR and QSR are applied in bearing fault diagnosis. The conclusions are as follows:

(i) MFPT first increases and then decreases as m and D increase, *i.e.*, the SR phenomenon occurs, and m is more sensitive to MFPT.

(ii) W also first increases and then decreases as D increases. Because the system has the double quad-stable's characteristics when $0 < m \leq 2$, the double peak of W occurs.

(iii) SAF is proportional to A and m, but is inversely proportional to f. Moreover, m is more sensitive to SAF and f has little effect on SAF.

(iv) According to simulation results, the amplification capability of QSR is superior than CTSR at low frequency ($f = 0.01$ Hz), high frequency ($f = 25$ Hz) and multi-frequency signals.

(v) According to simulation results, the SNR and MSNRI of QSR are about 2 times and 12 times higher than CTSR respectively, indicating better performance.

(vi) Under the 6205-2RS JEM SKF bearing fault detection, the amplitude of the inner and outer ring output signals of QSR is 3 times and 2 times higher than CTSR, respectively. For HRB 6205-2Z bearing fault detection, the amplitude of the inner and outer ring output signals of QSR is 13 times and 3 times higher than CTSR, respectively. And the SNR of QSR is larger than CTSR in both types of bearing fault. It shows that QSR is superior and has better noise immunity.

Future research will be focused on the theoretical analysis of the SNR and bearing fault detection under variable operating conditions.

Acknowledgements

Project supported by the National Natural Science Foundation of China (Grant No. 61771085) and the Research Project of Chongqing Educational Commission (Grant Nos. KJ1600407 and KJQN201900601).

References

[1] Li M D, Shi P M, Zhang W Y and Han D Y 2021 *Chaos, Solitons and Fractals* **151** 111228
[2] Zhang L, Lai L, Peng H, Tu Z and Zhong S H 2018 *Phys. Rev. E* **97** 012147
[3] Emanuel M, Miguel R G, Manuel C, Holger T G, Zhang Y H and Luis L B 2018 *Phys. Rev. Lett.* **121** 086805
[4] Xie M, Fan B, He X and Chen Q Q 2018 *Phys. Rev. E* **98** 052202
[5] Zamani A P, Novikov N and Gutkin B 2019 *Commun. Nonlinear Sci. Num. Simul.* **82** 105024
[6] Singh M, Verma A and Sharma N 2018 *Innovation and Research in Biomedical en* **39** 334
[7] Bai C Y 2018 *Physica A* **507** 304
[8] Evstigneev M, Pankov V and Prince R H 2001 *J. Phys. A: Gen. Phys.* **34** 2595
[9] Nurujjaman Md, Sekar Iyengar A N, Parmananda P 2008 *Phys. Rev. E* **78** 026406
[10] He L, Wu X, Zhang G 2019 *Physica A: Statistical Mechanics and its Applications* 545
[11] Liu Z P, Zhang J, Özdemir Ş K, Peng B, Jing H, Lü X Y, Li C W, Yang L, Nori F and Liu Y X 2016 *Phys. Rev. Lett.* **117** 110802
[12] Van der Groen Onno and Wenderoth Nicole 2016 *The Journal of Neuroscience* **36** 5289
[13] R Benzi, A Sutera and A Vulpiani 1999 *J. Phys. A* 14 L453
[14] Gammaitoni, Marchesoni, Menichella-Saetta and Santucci 1989 *Phys. Rev. Lett.* **62** 349
[15] Benzi R and Parisi G 2012 *Sutera A*
[16] McNamara and Wiesenfeld 1989 *Phys. Rev. A* **39** 4854
[17] Cheng Z, Hu N and Zuo M 2012 *J. Phys. Conference* **364** 012076
[18] Dykman M I, Luchinsky D G, Mannella R and Mcclintock PVE 1993 *J. Statist. Phys.* **70** 463
[19] Hanggi, Mroczkowski, Moss, McClintock 1985 *Phys. Rev. A* **32** 695
[20] Jung P and Hänggi P 1989 *Europhys. Lett.* **8** 505
[21] Jung Hänggi 1991 *Phys. Rev. A* **44** 8032
[22] Baomin Dai, Minxia Li and Yitai Ma 2014 *Appl. Thermal Eng.* **67** 283
[23] Liu J, Hu B, Yang F and Zang C L 2020 *Commun. Nonlinear Sci. Num. Simul.* **85** 105245
[24] Moreno Miguel V, Barci Daniel G and Arenas Zochil González 2020 *Phys. Rev. E* **101** 062110
[25] Xu L, Yu T, Lai L *et al.* 2020 *Commun. Nonlinear Sci. Num. Simul.* **83** 105133
[26] He L F, Cao L, Zhang G and Yi T 2018 *Chin. J. Phys.* **56** 1588
[27] Wang H, Obenauer-Kutner L and Lin M 2008 *J. Am. Chem. Soc.* **130** 8154
[28] Qiao Z J, Liu J, Ma X and Liu J L 2021 *Journal of the Franklin Institute* **358** 2194
[29] Lei Y, Qiao Z and Xu X 2017 *Mechanical Systems and Signal Processing* **94** 148
[30] He L F, Tan C L and Zhang G 2021 *The European Physical Journal Plus* **136** 1
[31] Sacco R L, Freddo L and Bello J A 1993 *W Archives of Neurology* **50** 609
[32] Ergin Y, Veli B, Matja P 2016 *Sci. China- Technological Sciences* **59** 364
[33] Jiao S B, Lei S, Jiang W, Zhang Q and Huang W C 2019 *IEEE Access* **7** 160191
[34] Morizono H, Ohishii Y and Yamamoto Y 2001 *J. Jpn. Soc. Clin. Cytol* **40** 500

[35] Zhang G, Wang H and Zhang T Q 2021 *Fluctuation and Noise Letters* **20** 2150045

[36] Qiao Z J, Elhattab A, Shu X D and He C B 2021 *Nonlinear Dynamics* **106** 707

[37] Lei Y G, Qiao Z J, Xu X F and Lin J 2017 *Mechanical Systems and Signal Processing* **94** 148

[38] Qiao Z J, Liu J, Xu X, Yin A M and Shu X D 2021 *Rev. Sci. Instrum.* **92** 105102

[39] Liu J J, Leng Y G, Fan S B *et al*. 2017 *American Society of Mechanical Engineers* **58226** V008T12A045

[40] Cheng W, Xu X M, Ding Y P and Sun K H 2020 *Rev. Sci. Instrum.* **91** 064701

[41] Zhang G, Tan C and He L 2021 *Mod. Phys. Lett. B* **35** 2150280

[42] Li J, Zhang J and Li M 2019 *Mechanical Systems & Signal Processing* **114** 128

[43] He L F, Hu D Y, Zhang G and Lu S L 2019 *Mod. Phys. Lett. B* **33** 19